IEICE Electronics Express, Vol.xx, No.xx, xx-xx

LETTER

Small magnetless integrated optical isolator using a magnetized cobalt ferrite film

Mario Alberto Serrano-Núñez [1a)], Yuya Shoji[1,2], and Tetsuya Mizumoto[1]

Abstract We experimentally demonstrated a silicon optical isolator using a monolithically integrated cobalt ferrite (CFO) film as magneto-optical material, achieving an isolation ratio of 9.6 dB near 1550 nm wavelength. By virtue of the large Faraday rotation coefficient of CFO, the device has a compact footprint comparing to the current yttrium iron garnet-based isolators. Further, we demonstrated self-biased isolation by the strong remanence of CFO films, eliminating the tedious demand of an external magnet. Cobalt ferrite represents a potential alternative approach to yttrium iron garnets to realize a practical device for on-chip isolation in silicon photonic integrated circuits because of the small footprint.

key words: Silicon photonics, optical isolators, micro ring resonators, magneto-optical materials, cobalt ferrite films.
Classification: Integrated optoelectronics

1. Introduction

Optical isolators allow propagation of light in photonic circuits in only one way, preventing backward light reflections to interfere in the stable operation of laser cavities or semiconductor optical amplifiers (SOA). The integration of optical isolators on semiconductor integrated platforms such as silicon (Si) remains as a persistent challenge for the photonics community. Several approaches to break Lorentz reciprocity and achieve on-chip isolation have been explored [1], such as spatial-temporal modulation of refractive index [2–4], nonlinear effects [5–7], or magneto-optical (MO) materials [8–11]. However, optical isolation based on some nonlinearities could be limited to a specific input power range when forward and backward propagating light are present simultaneously in the device [12], although this problem could be addressed by exploiting the thermal motion of hot atoms [13,14]. Similarly, modulation schemes typically require the use of complex and power-hungry drive circuitry, which is undesired for low-power consumption devices.

On the other hand, passive and truly nonreciprocal devices can be achieved using MO effects such as Faraday rotation, produced by magnetized MO materials. Cerium-substituted yttrium iron garnet (Ce:YIG), among other garnet ferrites, have been widely used in conventional discrete optic fiber systems owning to its low insertion loss and good MO effect at telecommunication wavelengths. However, the integration of Ce:YIG on semiconductor platforms such as silicon is difficult due to lattice and thermal expansion mismatches.

In order to solve this longstanding problem, two integration approaches have been predominantly investigated: heterogeneous [8,10,15], and monolithic [9,11,16,17]. The heterogeneous approach consists in the attachment by a bonding technology, of a Ce: YIG film epitaxially grown on a gadolinium gallium garnet (GGG) substrate on a silicon-on-insulator (SOI) waveguide. Although this method allows the use of a Ce:YIG film with a high figure of merit, devices fabricated via bonding usually have a remaining thick GGG substrate, which demands a relatively large chip area and complicates post-bonding fabrication steps. The monolithic approach consists in the deposition on a SOI waveguide assisted by a seed layer of a polycrystalline Ce:YIG film, reducing device footprint and simplifying fabrication process but sacrificing material quality. However, these films are typically recrystallized using thermal annealing process of over 800 ℃, which exceeds the convectional thermal budget of integrated semiconductor lasers (of around 500 ℃), possibly deteriorating their light-emitting properties and performance. On top of this, a magnetic field source to magnetize the Ce:YIG film such as a permanent film magnet [18], or an electromagnet [19,20], is required, adding more volume to the device and creating potential challenges for packaging.

In this letter, we demonstrate a monolithic and compact optical isolator on SOI, using a self-biased cobalt ferrite (CFO) film as an alternative MO material to conventional garnet ferrites. We recently demonstrated the crystalline deposition by a sputtering method of CFO films on Si substrates using a magnesium oxide (MgO)

[1] Department of Electrical and Electronic Engineering, Tokyo Institute of Technology, Meguro, Tokyo 152-8550, Japan
[2] FIRST, Tokyo Institute of Technology, Meguro, Tokyo 152-8550, Japan
a) serrano.m.aa@m.titech.ac.jp

DOI: 10.1587/elex.18.20210500
Received November 25, 2021
Accepted December 08, 2021
Publicized December 15, 2021

buffer layer [21]. Further, the Faraday rotation coefficient (θ_F) at 1,500 nm wavelength of our CFO films (25,600 deg/cm) is multiple times larger than the θ_F of epitaxial Ce:YIG films (-4,500 deg/cm [22]), reducing drastically the device footprint. What is more, owing to the strong remanent magnetization of CFO films, the present isolator can operate without an external magnet, reducing device bulk and improving fabrication throughput. In contrast to the material loss of epitaxial Ce:YIG of 5.8 dB/cm [23], the performance-limiting factor of CFO is its high material loss in the ~dB/μm order, caused by a strong concentration of Fe^{3+} and Co^{2+} absorptive cations. The material loss of CFO at 1550 nm wavelength is at least 0.7 dB/μm [24–26]. Nonetheless, in this article, we describe a compact device design having acceptably low insertion loss of ~3 dB with a proper cladding thickness and potential material loss reduction.

2. Device overview and fabrication method

The optical isolator is based on a Si racetrack resonator waveguide structure as illustrated in Fig. 1(a). The racetrack bending radius is 20 μm and the racetrack straight section length is 40 μm, featuring a reduced footprint of 40 x 80 μm aiming to reduce the inherit material loss induced by the CFO film. The Si racetrack is coupled to a single bus waveguide, with a bus-racetrack gap distance of 350 nm. A silica layer of 1-μm thickness is deposited on the structure as upper cladding. This silica cladding has a window on top of one of the racetrack straight sections, without fully exposing the waveguide structure to form a 250-nm thick "SiO_2 spacer" that keeps encapsulated the waveguide. A CFO (180 nm)/MgO (20 nm) film stack is deposited on top of the SiO_2 top cladding so that this material interacts with the waveguide optical mode only at the racetrack window region, forming a MO waveguide with a length (L_{MO}) of 40 μm (Fig. 1(b)). When the CFO film is magnetized in-plane and perpendicular to the propagating light direction by its own remanent magnetization, the resonant wavelengths (λ_r) between clockwise and counterclockwise propagating TM modes are split due to a nonreciprocal difference in their propagation constants. Such nonreciprocal resonant wavelength splitting ($\Delta\lambda$) is proportional to the MO activity of the CFO film and is described analytically as:

$$\Delta\lambda = \lambda \frac{\Delta n_{\text{eff}}}{n_g} \quad (1)$$

Where Δn_{eff} is the effective index variation and n_g is the average group index corresponding to the two propagating directions. The $\Delta\lambda$ can be estimated from the unperturbed TM mode profile of the MO waveguide using a perturbation theory together with the MO activity represented by the Faraday rotation of CFO [27]. A numerical simulation tool based on a finite-element method was used to obtain the unperturbed TM mode profile of the MO waveguide at 1550 nm wavelength (Fig. 1(c)). The geometry of the Si waveguide of the MO section was optimized to 450-nm width and 220-nm height, by maximizing the $\Delta\lambda$ of the device for the fundamental TM mode. The 250-nm thick silica spacer between CFO film and Si waveguide is expected to reduce the CFO material loss over 80% at the expense of reduced MO activity.

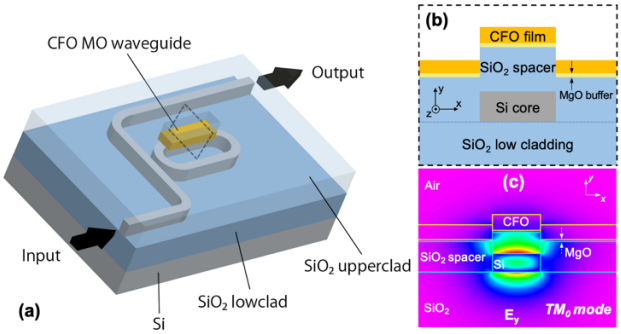

Fig. 1 (a) Schematic of the TM mode isolator using a CFO film. (b) Sketch of the cross-section of the MO racetrack waveguide. (c) Simulated E_y field distribution of the fundamental TM mode for the MO ring waveguide. Images are not to scale.

A microscopic picture of the device is shown in Fig. 2 (a). The Si racetrack structure is fabricated on an SOI wafer of Si(220 nm)/SiO_2(3 μm)/Si. A 200-nm thick SiO_2 mask layer was pre-deposited by a plasma-enhanced chemical vapor deposition (P-CVD) method. An electron-beam (EB) resist (ZEP520A) was coated and patterned with the device structure by EB lithography. Then, the pattern was transferred to the SiO_2 mask layer using a reactive ion etching (RIE) method in CF_4 plasma. Afterwards, the pattern was transferred to the Si layer via RIE in SF_6 plasma. Finally, the remaining SiO_2 mask layer was removed with an HF solution to complete the racetrack structure. Next, a 1-μm thick SiO_2 layer was deposited by P-CVD as upper cladding of the Si racetrack. Then, a window was opened on top of part of the racetrack structure to deposit a CFO film. The window pattern was transferred via maskless photolithography (based on AZ 5218 photoresist) and lift-off, to a 100-nm thick chromium (Cr) mask layer, previously deposited using a thermal deposition method. Subsequently, the window pattern was formed in the SiO_2 top cladding by RIE in CF_4 plasma. Without fully exposing the Si waveguide, a 250-nm thick SiO_2 spacer was formed to keep encapsulated the racetrack waveguide. The remaining Cr mask was removed with a chemical Cr remover. Finally, a CFO film with high θ_F was deposited on the structure using an MgO buffer layer as crystallization catalyst following the methods described in Ref.[21], forming a

MO waveguide section in the racetrack structure as shown in Fig. 2 (b).

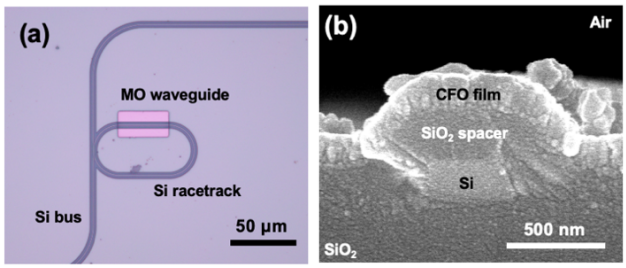

Fig. 2 (a) Optical microscopic picture of the fabricated device. (b) Cross-sectional SEM image of the MO racetrack waveguide.

3. Experimental results and discussion

We carried out isolation performance characterization to this device at near-infrared wavelengths by coupling TM-polarized light through the bus waveguide using a fiber-device-fiber setup [28]. Before measurement, the CFO film of the MO waveguide was magnetized for 10 minutes with an in-plane magnetic field of 20 kOe perpendicular to the light propagation direction, at a temperature of 100 ℃ and a pressure of 10^{-3} Pa. The applied H field is enough to saturate the sputtered CFO film, which almost reach its saturation magnetization of 330 emu/cm^3 with an H field of 15 kOe as shown in the magnetization hysteresis loop of a CFO film sputtered on Si substrate depicted in Fig. 3. The squareness ratio is defined as the ratio of the remanent magnetization (magnetization left in the medium after removing the magnetic field) to the saturation magnetization of the CFO film, which is around 33%.

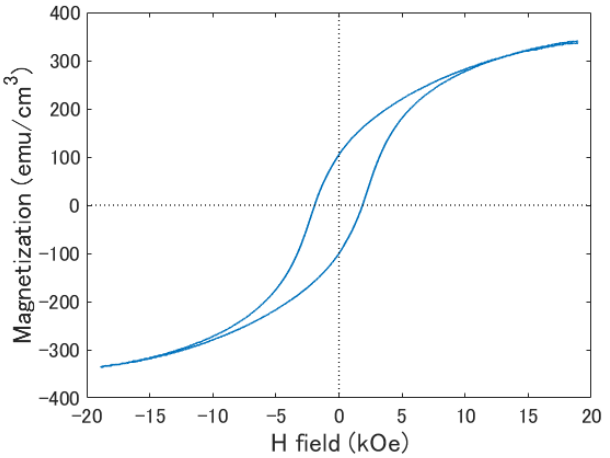

Fig. 3 In-plane magnetization hysteresis loop of deposited CFO film in a Si substrate at room temperature. The coercivity is 2 kOe, the saturation magnetization is 330 emu/cm^3, and the squareness ratio is 33%.

Fig. 4 plots the transmission spectra for TM-polarized light near 1550 nm wavelength, for both CW (blue) and CCW (red) propagation directions. It can be observed that the self-biased CFO film generated a TM resonance split between two propagating modes, achieving an isolation ratio (IR) of 9.6 dB at 1545.7 nm wavelength, with an insertion loss (IL) of 11.2 dB.

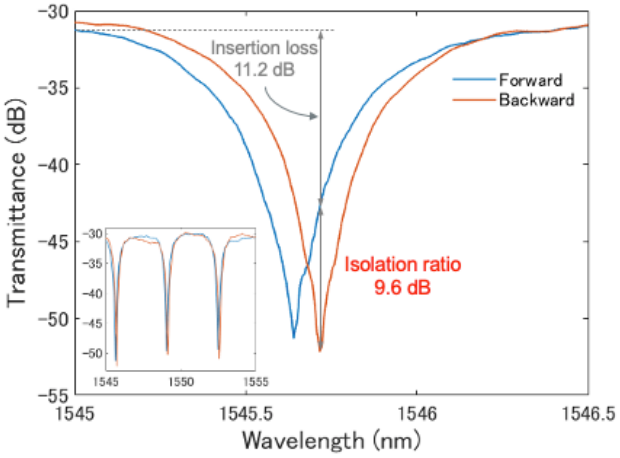

Fig. 4 Forward and backward transmission spectra of the fabricated isolator. The inset shows several adjacent resonant peaks in a wavelength range of 10 nm.

Using Eq. (1), we numerically estimated the nonreciprocal resonance splitting as a function of the Faraday rotation θ_F, which is plotted in Fig. 5. Considering the experimentally obtained $\Delta\lambda$ of 0.08 nm, its corresponding remanent θ_F is about 15,500 deg/cm. This value is in good agreement with the previously measured remanent θ_F of 14,000 deg/cm for a CFO/MgO film stack on a Si substrate [21]. The higher θ_F obtained could be attributed to the applied mild annealing, which could have released film residual stress, moving the magnetization easy axis slightly to the in-plane direction [29]. A further increment in the squareness ratio could lead to an improvement in the device isolation performance.

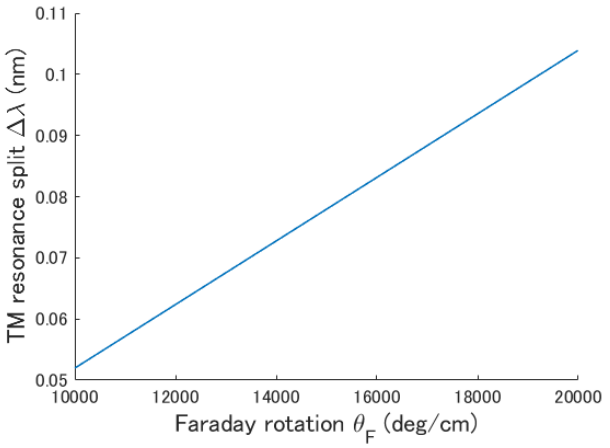

Fig. 5 Simulated nonreciprocal TM resonant wavelength split as function of Faraday rotation θ_F.

In order to estimate the optical loss of the CFO films, several Si waveguides with several window lengths (L_{MO}) were fabricated together with the racetrack isolator, in the same SOI wafer during the same process. By doing this, the MO waveguide cross-section shown in Fig. 2 (b) is the same across all the waveguides and the racetrack. The optical loss of the MO waveguide can be determined by measuring the waveguide loss of several window lengths. Fig. 6 plots the transmission loss at 1550 nm as a function of the L_{MO}. The transmission loss of a waveguide with no window was subtracted from the measured data. The CFO/MgO/SiO_2/Si waveguide propagation loss is determined to be 0.21 dB/μm. Since all the waveguide materials are considered low loss except for CFO, the CFO film material loss (α_{CFO}) can be inferred from its confinement factor (Γ) in the waveguide. Considering a simulated Γ of 6.1% for the CFO film, its corresponding α_{CFO} is 3.4 dB/μm with a standard error of 0.63 dB, which is conformal with other measurements in the ~dB/μm order previously reported as reviewed in the Introduction section.

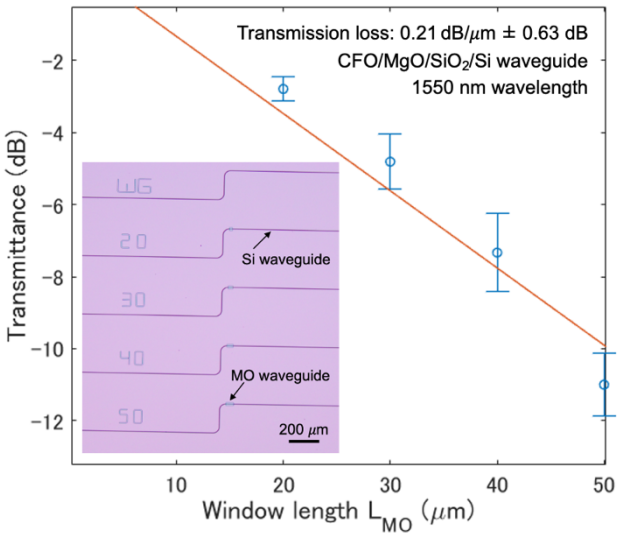

Fig. 6 The transmission loss of the CFO MO waveguide as a function of its length. Inset: Microscopic image of the fabricated Si waveguides with MO waveguides of several lengths.

To estimate the device insertion loss, we consider a lossless bus-ring coupling operating in an under coupled regime. The racetrack roundtrip loss per unit length (α_{ring}) is the sum of all internal racetrack loss contributions divided by the racetrack total length (L), and can be estimated using loaded quality factor (Q_{loaded}) with the relation [30]:

$$Q_{loaded} = \frac{\pi\lambda_r\sqrt{t\,exp(-\alpha_{ring}L/2)}}{FSR\sqrt{(1-t\,exp(-\alpha_{ring}L/2))}} \qquad (2)$$

Where FSR is the free spectral range of the racetrack. The self-coupling coefficient (t) is related to the bus-ring coupling coefficient (κ) as $t^2 + \kappa^2 = 1$. Considering an experimental Q_{loaded} of 2100, and a simulated κ of 10% corresponding to a bus-ring gap of 350 nm [31], the estimated α_{ring} is 51 dB/mm.

The main contributions to the ring roundtrip loss are propagation, junction, and bending losses. The propagation loss is determined by the summation of the Si waveguide and MO waveguide loss contributions. Since Si waveguides have a typical propagation loss in the ~dB/cm order [32], the propagation loss is governed mainly by the MO waveguide loss. For a device L_{MO} of 40 μm, the ring transmission loss is 8.4 dB. The junction loss was determined by evaluating the mode mismatch between the straight MO waveguide and the bending Si waveguide. Owing to the high confinement of the encapsulated Si waveguide, a small loss of 0.16 dB per junction was computed giving a total junction loss of 0.32 dB. Considering the relatively large device ring radius of 20 μm, a radiating bending loss lower than 0.001 dB per round was simulated. The total loss of these contributions is 8.7 dB, giving an α_{ring} of 43 dB/mm for a length L of 205 μm. This numerically estimated α_{ring} value is lower than the experimental value of 51 dB/mm as parasitic losses such as substrate loss, scattering loss, or surface scattering loss [33], are not considered in this calculation.

Fig. 7 shows the numerical calculations, as a function of the SiO_2 spacer height, of (a) nonreciprocal resonance split and loaded Q-factor, and (b) isolation ratio and insertion loss. A κ coefficient of 10% is considered since the coupling region is not modified. Notice that reducing the SiO_2 spacer height improves the resonance split as depicted by a blue line in Fig. 7(a). However, Fig. 7(b) shows that the isolation ratio (solid orange line) does not improve as $\Delta\lambda$ does due to an increment on the roundtrip loss caused by a higher mode confinement in the CFO film. This increment in the racetrack loss with a decreasing spacer height has an effect in the coupling regime, degrading the quality factor and the extinction ratio of the device and leading to a lower IR, even if $\Delta\lambda$ improves. Thus, a tradeoff is created when varying the SiO_2 spacer thickness between resonance split and Q-factor, as illustrated in Fig. 7(a). The ring geometry can be reengineered to improve these parameters and potentially improve IR. However, increasing the bus-ring power coupling and transmitting more light into the ring could result in a higher insertion loss due to the high α_{CFO}.

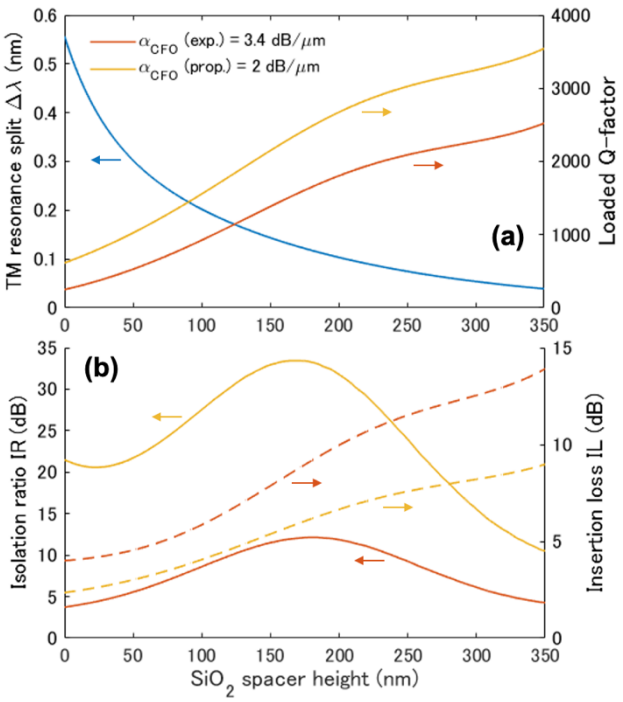

Fig. 7 (a) Simulated nonreciprocal TM resonant wavelength split (blue line) and loaded Q-factors for experimental (orange line) and proposed (yellow line) CFO material losses, as function of SiO_2 spacer height. (b) Simulated device isolation ratio (solid lines) and insertion loss (dashed lines) as function of SiO_2 spacer height, for experimental (orange lines) and proposed (yellow lines) CFO material losses. Experimental and proposed CFO material losses are 3.6 dB/μm and 2 dB/μm, respectively.

Another way to improve device performance is reducing the optical loss of CFO film. Supposing a CFO material loss of 2 dB/μm, a high IR with low IL is possible as shown by yellow lines in Fig. 7(b). For example, an IR of over 20 dB with an IL in the 3-dB order can be achieved with a SiO_2 spacer height of 50 nm. Given its reduced device footprint of 80 μm, a practical use of this isolator could be in an integrated SOA, where unidirectional optical amplification is needed. In this case, the bidirectional amplification nature of the gain medium would produce backward-traveling amplified spontaneous emissions, causing unwanted oscillation and other damages. Additionally, current integrated SOAs have good performance achieving high on-chip gains of up to 28 dB [34], tolerating the use of isolators with insertion losses of around 3 dB.

The substitution of Fe^{3+} cations in CFO with nonmagnetic metals such as Al^{3+} is a promising route to reduce α_{CFO} while improving the MO effect along the way [24,25]. Another approach is the use of CFO-based composite materials such as CFO nanoparticles embedded in a silica/zirconia matrix, achieving α_{CFO} values in the order of ~dB/cm [35]. However, the relatively low θ_F of current CFO composites hinders their application in real devices.

4. Conclusions

In conclusion, we experimentally demonstrated a compact TM mode isolator using a monolithically integrated cobalt ferrite film, achieving an isolation ratio of 9.6 dB at 1545.7 nm. The device is self-biased by the remanent magnetization of the CFO film, eliminating the need of an external magnet as magnetic field source. The ultra-reduced device footprint is owed to the remanent Faraday rotation coefficient of the CFO film, estimated to be 15,500 deg/cm near 1550 nm wavelength. The presented isolator solves the common problems of devices based on garnet ferrites, but the large cobalt ferrite material loss remains as a challenge. Despite the figure of merit as a ratio of MO effect and loss of garnet ferrite is still superior to that of CFO, the compact device size owing to its large θ_F and easier deposition are advantageous for on-chip isolation in silicon photonic integrated circuits.

Acknowledgments

This work was partially supported by the JST CREST #JPMJCR18T4; the JSPS KAKENHI #19H02190; the NEDO #JPNP13004 and #JPNP16007; and the Suematsu Fund.

References

[1] D. Jalas, *et al.*: "What is — and what is not — an optical isolator," Nat. Photonics. **7** (2013) 579 (DOI: 10.1038/nphoton.2013.185).

[2] D.B. Sohn, *et al.*: "Time-reversal symmetry breaking with acoustic pumping of nanophotonic circuits," Nat. Photonics. **12** (2018) 91 (DOI: 10.1038/s41566-017-0075-2).

[3] E.A. Kittlaus, *et al.*: "Electrically driven acousto-optics and broadband non-reciprocity in silicon photonics," Nat. Photonics. **15** (2021) 43 (DOI: 10.1038/s41566-020-00711-9).

[4] H. Tian, *et al.*: "Magnetic-free silicon nitride integrated optical isolator," Nat. Photonics. **15** (2021) 828 (DOI: 10.1038/s41566-021-00882-z).

[5] K.Y. Yang, *et al.*: "Inverse-designed non-reciprocal pulse router for chip-based LiDAR," Nat. Photonics. **14** (2020) 369 (DOI: 10.1038/s41566-020-0606-0).

[6] L. Del Bino, *et al.*: "Microresonator Isolators and Circulators Based on the Intrinsic Nonreciprocity of the Kerr Effect," Optica. **5** (2018) 279 (DOI: 10.1364/OPTICA.5.000279).

[7] L. Fan, *et al.*: "An all-silicon passive optical diode," Science (80-.). **335** (2012) 447 (DOI: 10.1126/science.1214383).

[8] Y. Shoji, *et al.*: "Magneto-optical isolator with silicon waveguides fabricated by direct bonding," Appl. Phys. Lett. **92** (2008) 071117 (DOI: 10.1063/1.2884855).

[9] L. Bi, *et al.*: "On-chip optical isolation in monolithically integrated non-reciprocal optical resonators," Nat. Photonics. **5** (2011) 758 (DOI: 10.1038/nphoton.2011.270).

[10] P. Pintus, *et al.*: "Microring-Based Optical Isolator and Circulator

with Integrated Electromagnet for Silicon Photonics," J. Light. Technol. **35** (2017) 1429 (DOI: 10.1109/JLT.2016.2644626).

[11] Y. Zhang, *et al.*: "Monolithic integration of broadband optical isolators for polarization-diverse silicon photonics," Optica. **6** (2019) 473 (DOI: 10.1364/optica.6.000473).

[12] Y. Shi, *et al.*: "Limitations of nonlinear optical isolators due to dynamic reciprocity," Nat. Photonics. **9** (2015) 388 (DOI: 10.1038/nphoton.2015.79).

[13] E.-Z. Li, *et al.*: "Experimental demonstration of cavity-free optical isolators and optical circulators," Phys. Rev. Res. **2** (2020) 1 (DOI: 10.1103/physrevresearch.2.033517).

[14] F. Song, *et al.*: "Optical nonreciprocity using four-wave mixing in hot atoms," Appl. Phys. Lett. **119** (2021) (DOI: 10.1063/5.0050628).

[15] S. Liu, *et al.*: "Mode-evolution-based TE mode magneto-optical isolator using asymmetric adiabatic tapered waveguides," Opt. Express. **29** (2021) 22838 (DOI: 10.1364/OE.427914).

[16] W. Yan, *et al.*: "Waveguide-integrated high-performance magneto-optical isolators and circulators on silicon nitride platforms," Optica. **7** (2020) 1555 (DOI: 10.1364/OPTICA.408458).

[17] C. Zhang, *et al.*: "Monolithically-Integrated TE-mode 1D Silicon-on-Insulator Isolators using Seedlayer-Free Garnet," Sci. Rep. **7** (2017) 5820 (DOI: 10.1038/s41598-017-06043-z).

[18] K. Okazeri, *et al.*: "Self-Holding Magneto-Optical Switch Integrated with Thin-Film Magnet," IEEE Photonics Technol. Lett. **30** (2018) 371 (DOI: 10.1109/LPT.2018.2791924).

[19] D. Huang, *et al.*: "Integrated broadband Ce:YIG/Si Mach–Zehnder optical isolators with over 100 nm tuning range," Opt. Lett. **42** (2017) 4901 (DOI: 10.1364/ol.42.004901).

[20] D. Huang, *et al.*: "Electrically driven and thermally tunable integrated optical isolators for silicon photonics," IEEE J. Sel. Top. Quantum Electron. **22** (2016) (DOI: 10.1109/JSTQE.2016.2588778).

[21] M.A. Serrano-Núñez, *et al.*: "Giant Faraday rotation of cobalt ferrite thin films deposited on silicon substrates for silicon photonic nonreciprocal device applications," Appl. Phys. Express. **13** (2020) 062002 (DOI: 10.35848/1882-0786/ab8b52).

[22] T. Shintaku: "Integrated optical isolator based on efficient nonreciprocal radiation mode conversion," Appl. Phys. Lett. **73** (1998) 1946 (DOI: 10.1063/1.122331).

[23] T. Shintaku, *et al.*: "Ce-substituted yttrium iron garnet films prepared on Gd3Sc2Ga3O12 garnet substrates by sputter epitaxy," Appl. Phys. Lett. **711** (1997) 1640 (DOI: 10.1063/1.1855460).

[24] J.W.D. Martens, *et al.*: "The polar magneto-optical Kerr effect and the dielectric tensor elements of CoFe 2− x Al x O 4 0.1≤ x ≤1 in the photon energy range 0.65≤ h ν≤4.5 eV," J. Appl. Phys. **55** (1984) 1100 (DOI: 10.1063/1.333199).

[25] K. Suzuki, *et al.*: "Preparation of zinc- and aluminum-substituted cobalt-ferrite thin films and their faraday rotation," Jpn. J. Appl. Phys. **27** (1988) 361 (DOI: 10.1143/JJAP.27.361).

[26] L. Bi, *et al.*: "Magneto-optical thin films for on-chip monolithic integration of non-reciprocal photonic devices," Materials (Basel). **6** (2013) 5094 (DOI: 10.3390/ma6115094).

[27] N. Bahlmann, *et al.*: "Improved design of magnetooptic rib waveguides for optical isolators," J. Light. Technol. **16** (1998) 818 (DOI: 10.1109/50.669010).

[28] E. Ishida, *et al.*: "Amorphous-Si waveguide on a garnet magneto-optical isolator with a TE mode nonreciprocal phase shift," Opt. Express. **25** (2017) 452 (DOI: 10.1364/oe.25.000452).

[29] G. Hu, *et al.*: "Structural tuning of the magnetic behavior in spinel-structure ferrite thin films," Phys. Rev. B - Condens. Matter Mater. Phys. **62** (2000) R779 (DOI: 10.1103/PhysRevB.62.R779).

[30] W. Bogaerts, *et al.*: "Silicon microring resonators," Laser Photonics Rev. **6** (2012) 47 (DOI: 10.1002/lpor.201100017).

[31] M. Bahadori, *et al.*: "Design Space Exploration of Microring Resonators in Silicon Photonic Interconnects: Impact of the Ring Curvature," J. Light. Technol. **36** (2018) 2767 (DOI: 10.1109/JLT.2018.2821359).

[32] X. Jiang, *et al.*: "Low-loss and low-crosstalk multimode waveguide bend on silicon," Opt. Express. **26** (2018) 17680 (DOI: 10.1364/oe.26.017680).

[33] M. Borselli, *et al.*: "Beyond the Rayleigh scattering limit in high-Q silicon microdisks: theory and experiment," Opt. Express. **13** (2005) 1515 (DOI: 10.1364/opex.13.001515).

[34] P. Kaspar, *et al.*: "Hybrid III-V/Silicon SOA in Optical Network Based on Advanced Modulation Formats," IEEE Photonics Technol. Lett. **27** (2015) 2383 (DOI: 10.1109/LPT.2015.2466543).

[35] F. Choueikani, *et al.*: "Self-biased magneto-optical films based on CoFe 2 O 4 –silica nanocomposite," J. Appl. Phys. **129** (2021) 023101 (DOI: 10.1063/5.0032620).